

Black hole spin and size of the X-ray emitting region(s) in the Seyfert 1.5 galaxy ESO 362–G18

B. Agís-González,^{1*} G. Miniutti,¹ E. Kara,² A.C. Fabian,² M. Sanfrutos,¹ G. Risaliti,^{3,4} S. Bianchi,⁵ N.L. Strotjohann,⁶ R. D. Saxton⁷ and M.L. Parker²

¹ *Centro de Astrobiología (CSIC–INTA), Dep. de Astrofísica; ESA, P.O: Box 78, E-28691, Villanueva de la Cañada, Madrid, Spain*

² *Institute of Astronomy, Madingley Road, Cambridge CB3 0HA*

³ *Harvard–Smithsonian Center for Astrophysics, 60 Garden St., Cambridge MA 02138, USA*

⁴ *INAF - Osservatorio Astronomico di Arcetri, L.go E. Fermi 5, Firenze, Italy*

⁵ *Dipartimento di Matematica e Fisica, Università degli Studi di Roma Tre, via della Vasca Navale 84, 00146 Roma, Italy*

⁶ *Physikalisches Institut, Universität Bonn, Nussallee 12, D-53115 Bonn, Germany*

⁷ *XMM SOC, ESA, P.O. Boc 78, E-28691, Villanueva de la Cañada, Madrid, Spain*

28 September 2018

ABSTRACT

We report results from multi–epoch X–ray observations of the Seyfert 1.5 galaxy ESO 362–G18 performed between November 2005 and June 2010. ESO 362–G18 generally exhibits the typical X–ray spectrum of type 1 Active Galactic Nuclei (AGN). A disc–reflection component accounts for broad residuals in the iron K band and above 10 keV, as well as for a significant soft excess. From our best–fitting reflection model, we measure a black hole spin $a \geq 0.92$ at the 99.99 per cent confidence level. ESO 362–G18 is also (typically) mildly absorbed by a column of neutral gas. The absorber is variable and one observation, performed ~ 2 months after a typical mildly absorbed one, is heavily absorbed by a cold column density of $\sim 3 - 4 \times 10^{23} \text{ cm}^{-2}$, nearly two orders of magnitude higher than that during any other observation. UV variability between the heavily absorbed observation and the others suggests that the absorber can be identified with a dusty, clumpy torus. The absorption variability timescale enables us to locate the X–ray emitting region within the innermost ~ 50 gravitational radii. Such result holds not only for the X–ray continuum, but also for the soft excess.

Key words: galaxies: active – X-rays: galaxies

1 INTRODUCTION

In recent years, several examples of X–ray absorption variability in Active Galactic Nuclei (AGN) have been reported on relatively short timescales ranging from hours to days (e.g. NGC 4388, Elvis et al. 2004; NGC 4151, Puccetti et al. 2007; NGC 1365, Risaliti et al. 2005; 2007; 2009 and Maiolino et al. 2010; NGC 7582, Bianchi et al. 2009; Mrk 766, Risaliti et al. 2011; SWIFT J2127.4+5654, Sanfrutos et al. 2013). The data are generally consistent with absorption by neutral/low–ionization clouds with typical column density of $10^{22} - 10^{24} \text{ cm}^{-2}$, number density of $10^9 - 10^{11} \text{ cm}^{-3}$, and velocity of few times 10^3 km s^{-1} which suggests that the variable X–ray absorber can be identified with broad line region (BLR) clouds. In the best studied cases, occultation events have been followed almost entirely from ingress to egress enabling e.g. Risaliti et al. (2007, 2009 in NGC 1365) and Sanfrutos et al. (2013 in SWIFT J2127.4+5654) to infer that the X–ray source is compact,

and confined within $5 - 10 r_g$ ($1 r_g = G M_{\text{BH}}/c^2$) around the central black hole.

X-ray absorption variability is also seen on longer timescales. These events are obviously more difficult to detect, as the longer timescale ideally requires long and continuous X–ray monitoring campaigns. In the few cases reported so far (e.g. Cen A, Rivers, Markowitz & Rothschild 2011; NGC 4507, Marinucci et al. 2012; ESO 323–G77, Miniutti et al. 2014; see Markowitz, Krumpke & Nikutta 2014 for a recent statistical analysis on such events) absorption on timescales of a few months can be attributed to clouds with typical column density of $10^{22} - 10^{23} \text{ cm}^{-2}$ and number density of $10^7 - 10^8 \text{ cm}^{-2}$, which points towards a clumpy torus origin (Nenkova et al. 2008a, 2008b).

Here we discuss the case of ESO 362–G18 (a.k.a. MCG 05–13–17), a Seyfert 1.5 galaxy at redshift $z = 0.012$ (e.g. Bennert et al. 2006). The X–ray luminosity from a *ROSAT* observation in the early 90s is $\sim 4 \times 10^{41} \text{ erg s}^{-1}$ in the 0.1–2.4 keV band, much lower than that required to model the extended narrow line region (ENLR) properties (Fraquelli, Storchi-Bergmann & Binette 2000).

* E-mail: agisgb@cab.inta-csic.es

Table 1. Details of the X-ray observations used in this work. The last two columns refer to the X-ray counts collected in a soft and hard energy band. The soft band is the 0.3–2 keV for the *Swift*, XMM 1 and XMM 2 observation, and the 0.5–2 keV for the *Suzaku* and the five *Chandra* observations. The hard band lower limit is set at 2 keV, while the upper bound is 10 keV except for the *Swift* and the five *Chandra* observations, where we use data up to 8.5 keV and 7.5 keV respectively because of signal-to-noise limitations.

Obs.	Obs. ID	Obs. date	Net exp.	$F_{0.5-2}$	F_{2-10}	Soft counts	Hard counts
Swift	00035234002	2005-11-26	7	3.9 ± 0.1	13.5 ± 0.4	1.7	1.0
XMM 1	0312190701	2006-01-28	8	0.66 ± 0.01	3.7 ± 0.1	4.3	2.1
Suzaku	703013010	2008-04-11	41	27.2 ± 0.1	33.2 ± 0.1	127.4	76.4
XMM 2	0610180101	2010-01-29	53	2.86 ± 0.02	9.58 ± 0.04	107.8	43.6
Chandra 1	11608	2010-05-18	10	2.67 ± 0.05	10.5 ± 0.2	6.5	3.9
Chandra 2	11609	2010-05-19	10	4.29 ± 0.06	13.3 ± 0.2	10.4	5.1
Chandra 3	11610	2010-05-21	10	2.11 ± 0.04	6.5 ± 0.2	5.3	2.5
Chandra 4	11611	2010-05-25	10	10.2 ± 0.1	19.9 ± 0.2	24.0	8.6
Chandra 5	11612	2010-06-03	10	6.55 ± 0.07	14.9 ± 0.2	15.2	5.8

The net exposure (fourth column) is in units of ks. Observed fluxes in the 0.5–2 keV (fifth column) and 2–10 keV bands (sixth column) are given in units of 10^{-12} erg s $^{-1}$ cm $^{-2}$. The soft and hard X-ray counts (last two columns) are in units of 10^3 photons.

This suggests that the *ROSAT* observation may have been affected by X-ray absorption, with different soft X-ray fluxes into our line-of-sight and into that of the ENLR. Subsequent observations with *Swift* and *XMM-Newton* confirm that X-ray absorption variability is present towards the X-ray-emitting region of ESO 362–G18, and that the soft X-ray luminosity during unabsorbed states is much higher than that derived by *ROSAT*. In fact, ESO 362–G18 makes a transition from an unobscured state with soft X-ray luminosity of $L_{0.5-2} \sim \text{few} \times 10^{42}$ erg s $^{-1}$ observed with *Swift* to a highly absorbed state with one order of magnitude lower soft luminosity observed with *XMM-Newton* about 2 months later (Winter et al. 2008).

We consider here 9 X-ray observations of ESO 362–G18 performed with the *Swift*, *XMM-Newton*, *Suzaku*, and *Chandra* X-ray observatories. The first 2 observations were performed only ~ 2 months apart (2005-11-26 and 2006-01-28 respectively), and the third was performed about 2.2 years later. The remaining 6 observations were all performed within one year (2010) in the framework of our dedicated X-ray monitoring of the source. In particular, the 5 *Chandra* monitoring observations were performed within 15 days, between 2010-05-18 and 2010-06-03. The most important details of the observations used in this work are given in Table 1. Results from further X-ray observations performed with *Swift* starting from November 2010 are reported elsewhere (Miniutti et al. in preparation), as they provide interesting, independent results by themselves.

2 X-RAY OBSERVATIONS

The data from the various missions and detectors have been reduced as standard using the dedicated software SAS v12.01 (*XMM-Newton*), CIAO v4.4 (*Chandra*), and HEASOFT v6.11 (*Swift* and *Suzaku*). Epoch- and position-dependent ancillary responses and redistribution matrices have been generated for each data set. Source products have been extracted from circular regions centered on the source, and background products have been generated from nearby source-free regions. For simplicity, we only consider here EPIC pn spectra from *XMM-Newton*, although we have checked their consistency with the MOS data. As for the *Suzaku* data, we merge the spectra from the front-illuminated CCD detectors XIS0 and XIS3 using the FTOOL ADDASCASPEC to obtain one single

front-illuminated CCD spectrum of the source. The resulting spectrum from the front-illuminated detectors is consistent with that from the back-illuminated XIS1 detector, although only the former is used here for simplicity. We also make use of the PIN data from the *Suzaku* HXD, which have been reduced with the dedicated FTOOL HXDGSOXBPI. The source flux obtained from the PIN detector is about 25 per cent of the background below 40 keV. Our *Chandra* observations were performed in continuous-clock mode to minimize pile-up and the resulting spectra are indeed pile-up free. When needed to convert fluxes into luminosities, we adopt a cosmology with $H_0 = 70$ km s $^{-1}$ Mpc $^{-1}$, $\Omega_\Lambda = 0.73$, and $\Omega_M = 0.27$. Quoted uncertainties refer to the 90 per cent confidence level for one interesting parameter unless otherwise stated.

3 X-RAY SPECTRAL VARIABILITY

As the five *Chandra* observations are part of a two-week long monitoring campaign, we shall treat them separately from the others to investigate any short-timescale spectral variability in detail (see Section 3.5). In order to first define a global X-ray spectral model to be used to study the spectral variability of ESO 362–G18, we start our analysis from the two highest-quality observations of our campaign, namely the *Suzaku* and the XMM 2 observations which provide, by far, the largest number of X-ray counts (see Table 1).

3.1 The high-resolution RGS data from the XMM 2 observation

As a first step, we examine the high-resolution spectrum from the RGS on board of *XMM-Newton* during the XMM 2 observation¹. We fit the RGS data with a simple blackbody plus power law and Galactic absorption model ($N_H = 1.75 \times 10^{20}$ cm $^{-2}$, Kalberla et al. 2005) which is adequate for the continuum. Several soft X-ray narrow emission lines are visually clear. We then add a series of

¹ The RGS data during the XMM 1 observation have poor quality due to the short exposure (~ 8 ks) and relatively low soft X-ray flux ($F_{0.5-2} \sim 6.4 \times 10^{-13}$ erg s $^{-1}$ cm $^{-2}$). On the other hand, the RGS data during the longer and higher-flux XMM 2 observation are of good enough quality to be used.

Table 2. The soft X-ray emission lines detected in the RGS spectrum of the XMM 2 observation. Line energies are given in keV, and intensities are reported in units of $10^{-5} \text{ ph s}^{-1} \text{ cm}^{-2}$.

Line ID	Lab. Energy	Observables	Measurements
N VII Ly α	0.500	Energy	0.49 ± 0.02
		Intensity	1.3 ± 0.6
O VII Ly α	0.561 (f)	Energy	0.561 ± 0.001
		Intensity	4.6 ± 1.0
	0.569 (i)	Energy	0.569 ± 0.002
		Intensity	1.2 ± 0.7
0.574 (r)	Energy	0.575 ± 0.002	
	Intensity	$0.7^{+1.0}_{-0.5}$	
O VIII Ly α	0.654	Energy	0.653 ± 0.002
		Intensity	1.3 ± 0.5

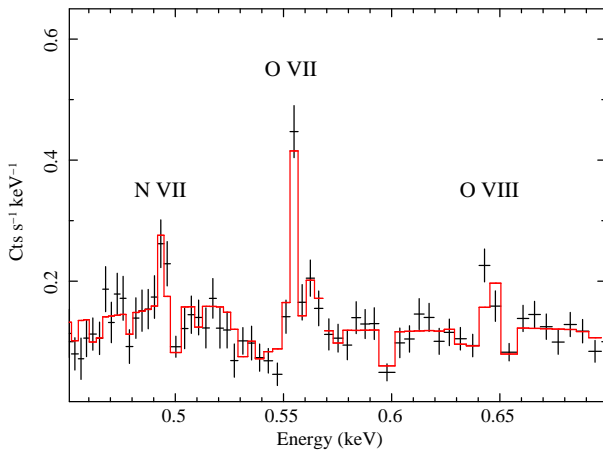


Figure 1. The RGS 1 spectrum obtained during the XMM 2 observation is shown together with the best-fitting model. The most important emission lines are labeled for reference (the O VII line being in fact a triplet). Data have been rebinned for visual clarity.

Gaussian emission lines, as required by the data. We detect 5 soft X-ray emission lines corresponding to N VII and O VIII Ly α , and to the O VII triplet. The properties of the detected lines are reported in Table 2. In Fig. 1, we show the most relevant portion of the RGS 1 spectrum together with the best-fitting model and the identification of the N VII, O VII (actually a triplet), and O VIII emission lines. The dominance of the forbidden O VII Ly α line at 0.561 keV strongly suggests emission by photo-ionized gas (e.g. Porquet & Dubau 2000). All subsequent spectral models include the emission lines of Table 2 with energy fixed at the laboratory value, and with normalization allowed to vary only within the uncertainties derived from the RGS analysis.

3.2 The high-quality *Suzaku* and XMM 2 observations

The X-ray spectra from the two high-quality observations (*Suzaku* and XMM 2) are shown in the upper panel of Fig. 2. In order to show the general spectral shape of the two observations, we fit a power law plus Galactic absorption model in the 1–4 keV and 7–10 keV bands, i.e. ignoring the soft and Fe K bands, as well as the *Suzaku* HXD data above 10 keV. The resulting data-to-model

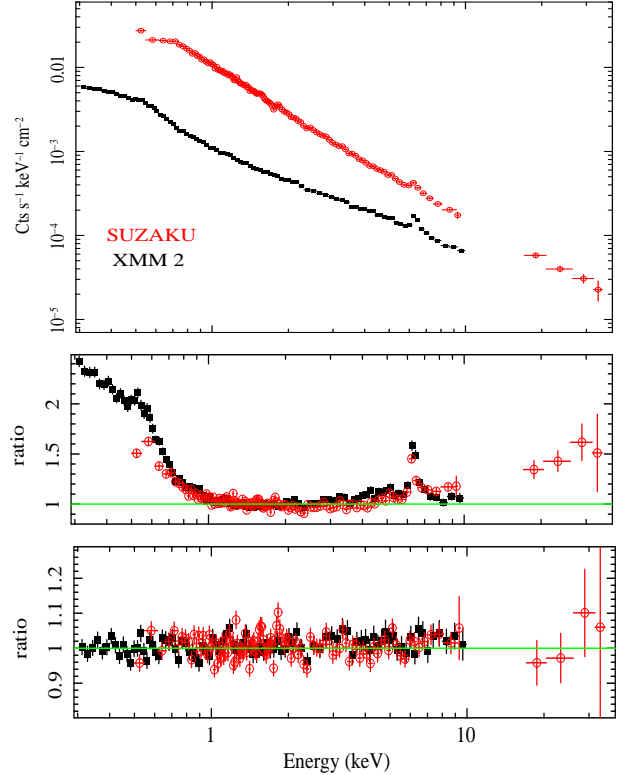


Figure 2. In the upper panel, we show the high-quality data from *Suzaku* (upper open circles, red in the on-line version) and XMM 2 (lower, filled squares). The two spectra are normalized to the different detector effective area to show the real spectral shape. In the middle panel, we show the data-to-model ratios obtained by fitting a power law absorbed by the Galactic column density in the 1–4 keV and 7–10 keV band (i.e. ignoring the soft excess, Fe K band, and hard X-ray data above 10 keV). This shows that both observations are characterized by a soft excess and exhibit broad residuals in the Fe K band. Moreover, the HXD/PIN data suggest the presence of a hard X-ray excess. In the lower panel, we show our final, broadband, best-fitting model, see text for details.

ratios are shown in the middle panel of Fig. 2. A soft excess with similar spectral shape is detected in both observations. Both spectra also exhibit broad residuals in the Fe K band, and the HXD/PIN data suggest that a hard X-ray excess is present above 10 keV. Note, however, that while the best-fitting photon index from the (higher flux) *Suzaku* observation is $\Gamma \simeq 2.0$, and in line with the typical spectral slope of unobscured AGN ($\Gamma > \simeq 1.9$, e.g. Piconcelli et al. 2005), the XMM 2 observation is extremely hard with $\Gamma \simeq 1.3$, possibly signaling that some extra component is needed in the hard band.

As a first step, we examine in some more detail the Fe K band spectra. Fitting a simple power law model (and Galactic absorption) in the 2–10 keV band, and ignoring the 4–7 keV energy range where Fe features are expected, produces the data-to-model ratio shown in the upper panel of Fig. 3. Adding an unresolved Gaussian with energy at 6.4 keV in the rest-frame accounts for the narrow Fe emission line and leaves a broad feature in the Fe K band (middle panel of Fig. 3). We then add a relativistic emission line model (the LAOR model, Laor 1991), and the data are now well reproduced in the 2–10 keV band with $\chi^2 = 1930$ for 1855 degrees of freedom (dof) (lower panel of Fig. 3). The narrow Fe emission line has an equivalent width of ~ 40 eV (~ 130 eV), and the broad relativistic one of ~ 130 eV (~ 250 eV) in the *Suzaku* (XMM 2) observation.

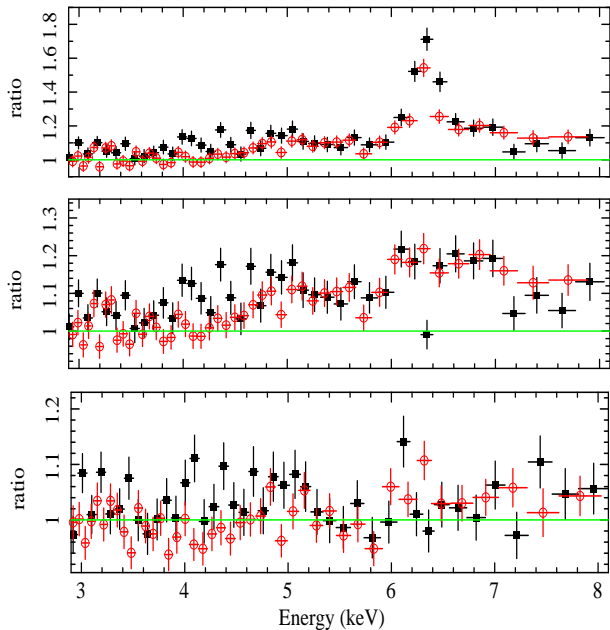


Figure 3. In the upper panel, we show the data-to-model ratio for the *Suzaku* and the XMM 2 observations in the Fe K band for a simple power law model fitted in the 2–10 keV band only and ignoring the 4–7 keV energy range (symbols are the same as in Fig. 2). In the middle panel, we account for the presence of an unresolved Fe emission line with a simple Gaussian model. A broad feature is left in the Fe K band in both observations. The feature is accounted for by an additional relativistic emission line model (lower panel).

As for the relativistic parameters (forced to be the same in the two observations), we obtain a disc inclination of $47^\circ \pm 8^\circ$, an emissivity index $q = 4.2 \pm 1.4$, and an inner disc radius of $\leq 3.1 r_g$ that, when identified with the innermost stable circular orbit around the black hole, corresponds to a black hole spin of $a \geq 0.76$. However, describing the data in a limited energy band with models that do not account for the reflection continuum associated with the emission lines may lead to misleading and/or inaccurate results. We then consider below a broadband spectral analysis using more self-consistent, physically-motivated spectral models.

Our broadband spectral model for both observations initially includes (i) a power law continuum, (ii) a distant reflection component (we use the PEXMON model in XSPEC, Nandra et al. 2007), (iii) all soft X-ray emission lines of Table 2, (iv) a disc-reflection component which may account for the soft excess, and for the positive residuals in the Fe K band (and in the HXD/PIN). The latter is modeled with the Ross & Fabian (2005) partially ionized reflection model² which is convolved with the KERRCONV relativistic kernel (Brenneman & Reynolds 2006) to account for any relativistic effects. The soft X-ray emission lines and the distant reflection component are forced to be the same in both spectra, as these components are not expected to vary.

The fit is relatively good with $\chi^2 = 3040$ for 2580 degrees of freedom (dof), and the disc-reflection component accounts well for all three features noted above, namely the soft excess, broad Fe K residuals, and hard X-ray excess. The description of the data improves by adding a rather typical warm absorber (we use the ZX-

² We extend their original grid to include values of the ionization parameter down to $\xi = 0.01 \text{ erg s}^{-1} \text{ cm}$ and photon indices down to $\Gamma = 1.5$.

IPCF model in XSPEC) affecting both the power law and the disc-reflection component. As the column density of the warm absorber is consistent with being the same in the two observations, we force a common N_{H} in both data sets. We obtain a significant improvement to $\chi^2 = 2880$ for 2577 dof with a common column density of $\simeq 10^{21} \text{ cm}^{-2}$ and $\log \xi \simeq 2.4$ ($\simeq 2.0$) for the *Suzaku* (XMM 2) observation. Although the fit is now acceptable, the XMM 2 data are not well reproduced with systematic positive residuals in the 2–6 keV band. Moreover, the resulting spectral shape for that observation is still rather flat ($\Gamma \simeq 1.5 - 1.6$) when compared with the typical value for unobscured AGN ($< \Gamma > \sim 1.9$).

We then consider the possible presence of absorption by including a neutral absorber affecting both the power law and disc-reflection components. For the sake of generality, we allow it to partially cover the X-ray source. The fit improves dramatically by $\Delta\chi^2 = -137$ for 4 more free parameters ($\chi^2 = 2743$ for 2573 dof). In fact, the *Suzaku* spectrum is consistent with being unabsorbed (with covering fraction ≤ 0.1). Hence, the improvement is only due to a better description of the XMM 2 spectrum which requires a neutral absorber with column density $N_{\text{H}} \simeq 10^{22} \text{ cm}^{-2}$ and covering fraction $C_f \simeq 0.4$. The photon index during the XMM 2 observation is now $\Gamma \simeq 1.8$, broadly consistent with a standard spectral slope. Replacing the disc-reflection component with a phenomenological blackbody (or disc blackbody) model to account for the soft excess results in a much worse statistical description of the data ($\chi^2 = 2938$ for 2576 dof), demonstrating that the disc-reflection model is a better description for the soft excess.

Let us discuss here results on the relativistic parameters associated with the disc-reflection component, namely the black hole spin a , emissivity index q , and disc inclination i . The error contour for the black hole spin is shown in the upper panel of Fig. 4. We measure a black hole spin of $a \geq 0.92$ at the 99.99 per cent confidence level, and of ≥ 0.98 at the 90 per cent one. Hence, the accreting black hole powering ESO 362-G18 is a very rapidly spinning Kerr black hole, consistent with being maximally spinning ($a = 0.998$). The contours plot for the disc-reflection emissivity index (q) and for the disc inclination (i) is shown in the lower panel of the same Figure and indicates that $q = 4.3_{-0.6}^{+0.8}$ and $i = 53^\circ \pm 5^\circ$ (90 per cent confidence level for the two interesting parameters). All three parameters are consistent with those derived from the simpler analysis discussed above and performed with emission line models only (see Fig. 3 and the associated discussion). However, using the broadband data and more self-consistent and physically-motivated models significantly reduces the uncertainties on these relevant parameters.

3.3 Joint fits to the *Swift*, *Suzaku* and the two XMM-Newton spectra

Having found a good global spectral model for the two highest-quality observations of our campaign, we now use it to perform a simultaneous analysis of the first four X-ray observations of Table 1, namely to the *Swift*, XMM 1, *Suzaku*, and XMM 2 observations. We defer the analysis of the five *Chandra* monitoring observations to Section 3.5. The X-ray spectrum of ESO 362-G18 from the first four observations is shown in the upper panel of Fig. 5 together with the best-fitting models (see below). Remarkable spectral variability is present with a general steeper-when-brighter behavior. Moreover the (lowest flux) XMM 1 observation appears to have a distinct spectral shape. The visually larger narrow Fe line equivalent width suggests that the hard X-ray continuum is significantly

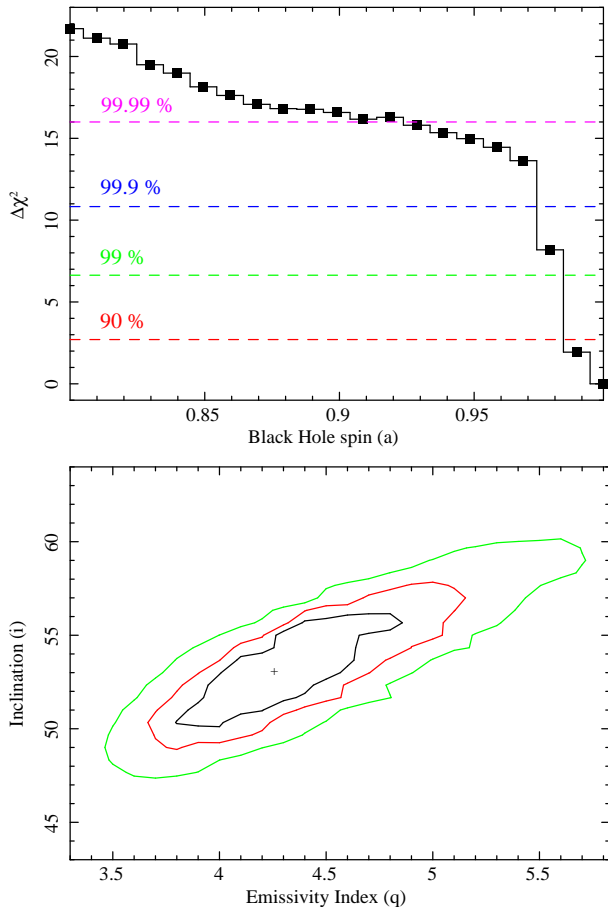


Figure 4. In the upper panel, we show the error contour for the black hole spin in ESO 362–G18, as obtained from the disc reflection model applied to the two high-quality observations (*Suzaku* and XMM 2). The contour has been obtained allowing all other model parameters to vary. The horizontal dashed lines are, from bottom to top, the 90, 99, 99.9, and 99.99 per cent confidence levels. Values of $a \leq 0.8$ always give $\Delta\chi^2 \geq 22$, and are not shown for visual clarity. In the lower panel, we show the 68, 90, and 99 per cent confidence level contours for the disc–reflection emissivity index and for the disc inclination. The contours have been obtained allowing all other parameters to vary.

depressed during the XMM 1 observation, either because of an intrinsic low flux state or because of absorption.

We proceed by performing a joint fit to the four observations with the same model discussed above. The warm absorber ionization is unconstrained during the *Swift* and XMM 1 observations. We then fix this parameter to that obtained during the higher quality XMM 2 observation which (according to our best-fitting model, see below) has a similar intrinsic luminosity. We force the warm absorber column density to be the same in all observations, as in the analysis of the high-quality *Suzaku* and XMM 2 observations. The joint fit is excellent with $\chi^2 = 3140$ for 2933 dof. The most remarkable result is that the lowest-flux XMM 1 observation appears to be heavily absorbed by neutral gas with a column density of $\simeq 10^{23} \text{ cm}^{-2}$ covering about 80 per cent of the X–ray source. Removing the absorber from the XMM 1 model, i.e. attempting to explain the XMM 1 spectral shape with no intrinsic absorption (beside the warm absorber), yields to a disc–reflection dominated model but results in a poorer statistical description ($\chi^2 = 3162$ for 2936 dof). Moreover, the photon index is too flat to be realistic

($\Gamma \sim 1.5$). We conclude that the spectral shape during the XMM 1 observation is driven by cold absorption rather than by an extremely low intrinsic flux.

Some residuals are seen at ~ 0.9 keV during the lowest flux XMM 1 observation. Adding a further soft (unresolved) X–ray emission line at 0.904 keV (corresponding to Ne IX Ly) yields $\Delta\chi^2 = -34$ for 1 more free parameter (although it was not detected in our analysis, the line intensity is consistent with the RGS spectrum of the XMM 2 observation, and it is included with the same intensity of $1.8 \times 10^{-5} \text{ ph s}^{-1} \text{ cm}^{-2}$ in all observations, as is the case for all other unresolved soft X–ray emission lines, see Table 2). The soft X–ray emission lines we include in our model are most likely associated with emission from extended gas that is photo-ionized by the AGN. The same gas may also be associated with a soft scattered component, as ubiquitously seen in the X–ray spectra of heavily absorbed AGN (e.g. Bianchi et al. 2005). We test this scenario by adding to our model a soft power law that is only absorbed by the Galactic column density. Its normalization is the same in all spectra, as this component is not expected to vary. The fit does not improve ($\Delta\chi^2 = -3$ for 2 more free parameters). We measure a photon index $\Gamma \simeq 2.4$ and a scattered 0.5–2 keV luminosity of $\sim 10^{41} \text{ erg s}^{-1}$. This component is overwhelmed by the X–ray continuum, and thus negligible, in all observations except the lowest-flux XMM 1 observation. For consistency with the typical soft X–ray spectrum of heavily obscured AGN, we keep this component in our best-fitting spectral model although, as mentioned, it is not formally required by the data.

We conclude that most of the spectral variability seen in the upper panel of Fig. 5 is due to a variable cold absorber changing in both column density and covering fraction, although photon index variability is also detected with $\Delta\Gamma \sim 0.2 - 0.3$. The most important absorption variability event is detected during the XMM 1 observation which requires a much higher level of neutral X–ray absorption than any other observation and, in particular, than the *Swift* observation which was performed only 63 days earlier. We measure a column density of $\simeq 10^{23} \text{ cm}^{-2}$ covering $\simeq 80$ per cent of the X–ray emitting regions during the XMM 1 observation. Such a column density is more than one order of magnitude higher than during any other observation.

3.4 A hard scattered component

As discussed extensively by Miniutti et al. (2014), the inclusion of a hard scattered component describes very well the absorbed X–ray states of another source which exhibits extreme X–ray absorption variability, namely ESO 323–G77. A hard scattered component is likely present in all cases where absorption is due to a clumpy rather than homogeneous structure. This is because our line-of-sight (LOS) is absorbed by a specific clump (cloud), but the X–ray continuum in different directions intercepts different clumps which re-direct part of it into our LOS via scattering. The presence of a hard scattered component has also been reported in other absorbed AGN such as NGC 3227 (Lamer, Uttley & McHardy 2003) and NGC 7582 (Piconcelli et al. 2007). Both sources exhibit variable X–ray absorption, most likely associated with clumpy absorbers, in line with the scattering interpretation outlined above. The X–ray absorption variability ESO 362–G18 strongly suggests that this is the case here as well.

In order to check for the presence of a hard scattered component in ESO 362–G18, we use the same phenomenological model used by Miniutti et al. (2014) for the case of ESO 323–G77. We include an additional absorbed power law with the same

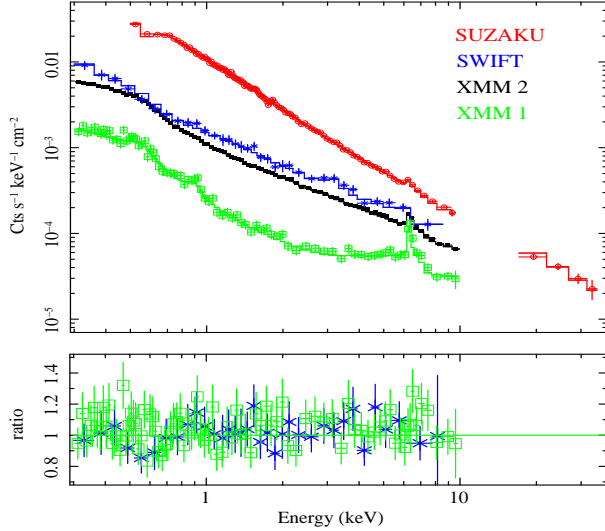


Figure 5. In the upper panel, we show the data and best-fitting models for the first four observations of our campaign (see Table 1). Each spectrum is re-normalized to the effective area of the corresponding detector. From top to bottom, we show the *Suzaku*, *Swift*, XMM 2, and XMM 1 data. In the lower panel, we show the best-fitting data-to-model ratios for the *Swift* and XMM 1 observations. The corresponding plot for the *Suzaku* and XMM 2 observations has already been shown in the lower panel of Fig. 2, and it is not reproduced here for visual clarity.)

(observation-dependent) photon index and normalization as the intrinsic nuclear continuum, we allow the column density towards this component to be different than that affecting the nuclear continuum (but the same in all observations), and we multiply the model by a constant allowed to vary between 0 and 1 which represents the hard scattering fraction. The statistical description of the data improves significantly by $\Delta\chi^2 = -28$ for 2 more free parameters for a final result of $\chi^2 = 3075$ for 2928 dof. The hard scattered component is absorbed by a column density of $\sim 2 - 3 \times 10^{22} \text{ cm}^{-2}$, and its scattering fraction is ~ 12 per cent. Note that this component is significantly detected only during the most heavily absorbed XMM 1 observation (as expected, see the discussion in Miniutti et al. 2014). The inclusion of that component induces a higher column density and covering fraction during the XMM 1 observation, while not affecting any other parameter. We now measure a column density of $\sim 3 - 4 \times 10^{23} \text{ cm}^{-2}$, consistent with a full coverage of the X-ray emitting region with covering fraction $C_f \geq 0.94$ during the XMM 1 observation. Note that, as our phenomenological description of the hard scattered component is likely only a rough approximation of the true spectral shape, these values are likely affected by larger uncertainties than the quoted statistical ones.

Re-running the error contours on the relativistic parameters (see Fig. 4) gives identical results. This is expected since the relativistic parameters are best constrained from the highest-quality X-ray spectra that are basically unaffected by the inclusion of the hard scattered component. The final best-fitting results are reported in Table 3 and a summary and brief discussion of the main results is presented in Section 4. The data-to-model ratios for the *Swift* and XMM 1 observations are shown in the lower panel of Fig. 5 (see Fig. 2 for the *Suzaku* and XMM 2 observations). As an example of the overall spectral model, the best-fitting model for the mildly absorbed XMM 2 observation is shown in Fig. 6 together with all spectral components.

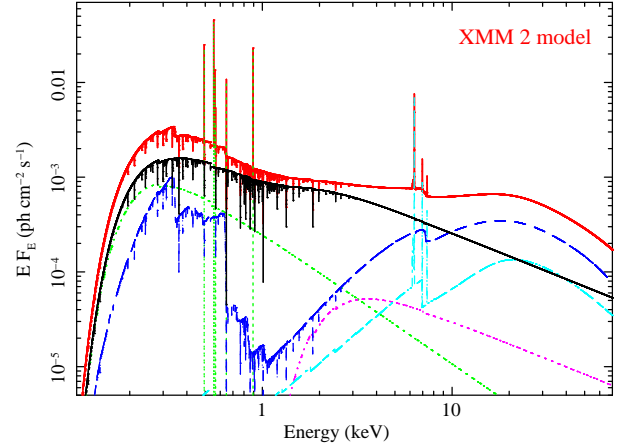


Figure 6. The best-fitting model for the XMM 2 observation (upper solid line, red in the on-line version) together with all spectral components. The black solid line is the intrinsic power law, affected by both warm and cold (partially covering) absorption. The disc-reflection component is the dashed line (dark blue in the on-line version), while the dash-dotted line represents the distant reflection component (light blue in the on-line version). Dotted lines show the scattered components, comprising a soft scattered power law plus emission lines (green in the on-line version), and an absorbed, hard scattered component that has a luminosity of ~ 12 per cent that of the intrinsic continuum. Note that the latter component has a negligible contribution in the XMM 2 observation and that it is significantly detected only in the most absorbed XMM 1 observation, as discussed in the text.

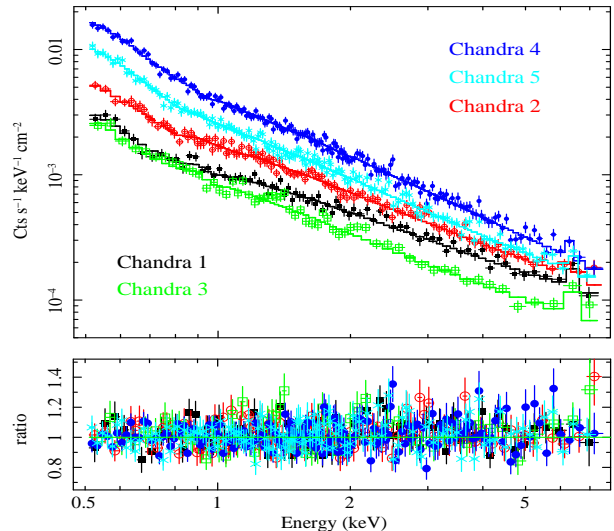


Figure 7. In the upper panel, we show the data and best-fitting models for the five *Chandra* monitoring observations performed within 15 days from 2010-05-18 to 2010-06-03. In the lower panel, we show the best-fitting data-to-model ratios resulting from the joint fit to the five data sets.

3.5 The two weeks *Chandra* monitoring campaign

We consider here a joint fit to the five *Chandra* monitoring observations performed between 2010-05-18 to 2010-06-03 using the same X-ray spectral model described above. We fix the parameters associated with the soft X-ray emission lines, the distant reflection component, and the soft and hard scattered components to the values derived from the analysis discussed above, as the *Chandra* data have typically lower spectral quality, and because these

components are not expected to vary. The relativistic parameters affecting the disc reflection component are also fixed to the best-fitting values obtained from the analysis of the first four observations, as the *Chandra* data cannot constrain them any better. As before, we force the warm absorber column density to be the same in all observations, while the ionization parameter is free to vary independently. As for the neutral partial covering absorber, the column density is initially free to vary independently. However, as N_{H} turns out to be consistent with being the same in all *Chandra* observations, we force it to have the same value in all data sets, so that the cold absorber is only allowed to vary in covering fraction.

We reach a good statistical description of the five *Chandra* monitoring observations with a final result of $\chi^2 = 1248$ for 1218 dof. The spectra, best-fitting models, and final data-to-model ratios for the joint fit to the five data sets are shown in Fig. 7. The observed spectral variability can be explained by a combination of photon index variability ($\Delta\Gamma \simeq 0.3$, although the relatively large 90 per cent uncertainties imply that $\Gamma = 1.9 - 2.0$ is an acceptable solution for all observations) and by moderate changes in the covering fraction of a cold absorber with column density of $\simeq 8 \times 10^{21} \text{ cm}^{-2}$. Our best-fitting results are reported in Table 3 and discussed in Section 4. We conclude that absorption variability, if present at all, is only modest during the two weeks *Chandra* monitoring campaign. Hence, the shortest timescale absorption variability event we detect is that occurring within the two months separating the *Swift* and the XMM 1 observations.

4 SUMMARY OF THE MULTI-EPOCH SPECTRAL ANALYSIS

The relevant best-fitting parameters of our multi-epoch spectral analysis are reported in Table 3. The parameters associated with the soft emission lines, the soft/hard scattering components, the distant reflector, and the disc-reflection relativistic kernel are the same in all observations. They are reported in the upper part of the Table. As mentioned, these parameters have been fixed in the joint analysis of the *Chandra* observations, so that the reported values and errors are drawn from the joint fit to the *Swift*, XMM 1, *Suzaku*, and XMM 2 observations.

A disc-reflection component is detected in all observations, except the *Swift* and *Chandra* 3 ones, where only upper limits are obtained. This is likely because of the relatively low spectral quality of these observations (see Table 1). The relativistic parameters are best constrained from the highest-quality spectra (*Suzaku* and XMM 2) and suggest that ESO 362–G18 is powered by a very rapidly spinning Kerr black hole (with spin $a \geq 0.98$ at the 90 per cent confidence level). The observer inclination with respect to the disc axis is also very well constrained ($i \sim 53^\circ$). The disc ionization state is rather low, and we are only able to obtain upper limits on the ionization parameter, except during the highest flux *Suzaku* and *Chandra* 4 observations.

The intrinsic photon index Γ is variable and it appears to be steeper during the highest flux observations (*Suzaku* and *Chandra* 4), consistent with a steeper-when-brighter behaviour. After checking that the data allow us to do so, the warm absorber column density is forced to be the same during the first four and during the subsequent five observations. The final results indicate that the warm absorber column density is in fact likely constant during the whole 2005–2010 campaign with $N_{\text{H}} \simeq 1 - 2 \times 10^{21} \text{ cm}^{-2}$. On the other hand, the warm absorber ionization is marginally variable and roughly consistent with responding to the intrinsic variability

although the relatively large errors do not allow us to investigate its variability in detail.

A neutral, partially covering absorber is detected in all observations but the *Suzaku* one, which appears to be unabsorbed. The absorber is variable, and the X-ray spectrum of ESO 362–G18 changes from unabsorbed or only mildly absorbed states (e.g. during the *Swift* and *Suzaku* observation) to highly absorbed ones (the XMM 1 observation), going also through states with intermediate levels of absorption (the remaining XMM 2 and *Chandra* observations). The most remarkable absorption variability event is that occurring over the 63 days separating the mildly absorbed *Swift* observation ($N_{\text{H}} \sim 5 \times 10^{21} \text{ cm}^{-2}$ and $C_f \simeq 0.5$) and the heavily absorbed XMM 1 one ($N_{\text{H}} \simeq 3 - 4 \times 10^{23} \text{ cm}^{-2}$ and $C_f \geq 0.94$).

5 THE BLACK HOLE MASS AND FURTHER, INDEPENDENT CONSTRAINTS ON THE SYSTEM INCLINATION

García-Rissmann et al. (2005) measure the stellar velocity dispersion of ESO 362–G18 from the Calcium triplet obtaining $\sigma_* = 130 \pm 4 \text{ km s}^{-1}$ (we consider the average value and standard deviation of their two measurements). The black hole mass can be estimated from the $M_{\text{BH}} - \sigma_*$ relation (e.g. Merritt & Ferrarese 2001; Tremaine et al. 2002). Using the $M_{\text{BH}} - \sigma_*$ relationship as obtained by Xiao et al. (2011), we estimate a black hole mass of $M_{\text{BH}} = (0.8 - 1.7) \times 10^7 M_\odot$. However, in order to include the spread and not only the statistical uncertainties on the best-fitting $M_{\text{BH}} - \sigma_*$ relation, we prefer to consider the sample of reverberation-mapped AGN from Woo et al. (2010) that have stellar velocity dispersion consistent with that of ESO 362–G18, and to assign to our AGN the black hole mass range that can be derived from this sub-sample. With this prescription, we obtain a larger mass range of $M_{\text{BH}} = (0.7 - 7.2) \times 10^7 M_\odot$.

Another estimate of the black hole mass can be obtained by combining the observed optical luminosity with the $\text{H}\beta$ broad emission line FWHM by using, e.g. the relationship from Park et al. (2012), i.e.

$$M_{\text{BH}} = A \left(\frac{\text{FWHM}_{\text{H}\beta}}{10^3 \text{ km s}^{-1}} \right)^{1.666} \left(\frac{\lambda L_{5100}}{10^{44} \text{ erg s}^{-1}} \right)^{0.518}, \quad (1)$$

where $A = 10^{6.985} M_\odot$. Bennert et al. (2006) report a $\text{H}\beta$ FWHM = $5240 \pm 500 \text{ km s}^{-1}$ from the optical spectrum obtained at the New Technology Telescope (NTT) on 2004–09–17. They also measure a nuclear 5100 Å luminosity of $\sim 4.1 \times 10^{43} \text{ erg s}^{-1}$. By using Eq. 1, we then have $M_{\text{BH}} = (0.8 - 8.1) \times 10^8 M_\odot$, which appears to be inconsistent (and much higher) than that derived from the stellar velocity dispersion.

However, Eq. 1 assumes an average virial coefficient $\log f = 0.72$, as derived by Woo et al. (2010). In fact, f is likely source-dependent, and depends on the unknown BLR geometry. If we assume a disc-like BLR geometry, the virial relationship can be expressed in terms of line FWHM as

$$M_{\text{BH}} = R_{\text{BLR}} \text{FWHM}^2 (4G \sin^2 i)^{-1}, \quad (2)$$

where i is the inclination between the LOS and the angular momentum of the disc-like BLR, whose direction is likely parallel to that of the accretion flow angular momentum. R_{BLR} can be estimated from the Bentz et al. (2009) BLR-luminosity relationship which, for the given 5100 Å luminosity gives $R_{\text{BLR}} \sim 5.2 \times 10^{16} \text{ cm}$. Our disc-reflection model provides information on the system inclination, namely $i = 53^\circ \pm 5^\circ$. Inserting R_{BLR} and i into the

Table 3. Best-fitting parameters for the multi-epoch analysis. The constant continuum components (upper part of the Table) comprise the soft and hard scattered power law as well as the distant reflection component. $L_{0.5-2}^{(ss)}$ is the luminosity of the soft scattered (ss) component, comprising contributions from the soft scattered power law and from all unresolved soft X-ray emission lines. $N_{\text{H}}^{(hs)}$ and $f^{(hs)}$ are the column density towards the hard scattered component and its scattering fraction. The superscript $^{(XMM2)}$ means that the parameter is tied to that during the XMM 2 observation. Luminosities are unabsorbed and given in units of 10^{42} erg s^{-1} ; column densities are given in units of 10^{22} cm^{-2} ; the ionization parameter is given in units of erg cm s^{-1} .

Constant continuum components and common relativistic parameters								
Soft scattering		Hard scattering		Distant reflection	Disc-reflection relativistic parameters			
$\Gamma^{(ss)}$	$L_{0.5-2}^{(ss)}$	$N_{\text{H}}^{(hs)}$	$f^{(hs)}$	$L_{2-10}^{(ref)}$	a	q	i	
2.4 ± 0.1	0.12 ± 0.05	2.5 ± 1.6	$0.12^{+0.08}_{-0.06}$	0.32 ± 0.09	≥ 0.98	$4.3^{+0.8}_{-0.6}$	53 ± 5	
Variable components								
Obs.	Cold absorber		Warm absorber		Continuum	Disc-reflection		
	$N_{\text{H}}^{(cold)}$	$C_{\text{f}}^{(cold)}$	$N_{\text{H}}^{(ion)}$	$\log \xi$	Γ	$L_{2-10}^{(nuc)}$	$\xi^{(ref)}$	$L_{2-10}^{(ref)}$
Swift	0.5 ± 0.4	0.5 ± 0.3	0.15 ± 0.04	$2.0^{(XMM2)}$	2.0 ± 0.4	2.0 ± 0.3	≤ 25	≤ 2.0
XMM 1	35 ± 8	≥ 0.94	"	$2.0^{(XMM2)}$	1.90 ± 0.09	2.3 ± 0.2	≤ 32	$0.9^{+0.5}_{-0.7}$
Suzaku	≤ 3	≤ 0.1	"	2.4 ± 0.2	2.12 ± 0.03	8.35 ± 0.08	16 ± 12	1.9 ± 0.2
XMM 2	1.3 ± 0.2	0.42 ± 0.04	"	2.0 ± 0.3	1.80 ± 0.04	1.95 ± 0.06	≤ 8	0.9 ± 0.1
$\chi^2/\text{dof} = 3075/2928$								
Chandra 1	0.8 ± 0.2	0.6 ± 0.1	0.20 ± 0.08	2.0 ± 1.1	1.7 ± 0.2	2.3 ± 0.2	≤ 26	0.7 ± 0.5
Chandra 2	"	0.4 ± 0.1	"	1.9 ± 0.6	1.8 ± 0.2	3.1 ± 0.1	≤ 25	0.9 ± 0.4
Chandra 3	"	0.5 ± 0.2	"	2.5 ± 1.3	1.8 ± 0.3	1.2 ± 0.4	≤ 35	≤ 1.6
Chandra 4	"	0.48 ± 0.06	"	2.5 ± 0.4	2.1 ± 0.1	4.9 ± 0.1	7 ± 6	1.3 ± 0.3
Chandra 5	"	0.4 ± 0.1	"	2.1 ± 0.4	2.0 ± 0.1	3.4 ± 0.1	≤ 19	1.1 ± 0.2
$\chi^2/\text{dof} = 1248/1218$								

virial relationship leads to a black hole mass estimate of $M_{\text{BH}} = (4.5 \pm 1.5) \times 10^7 M_{\odot}$, which is now totally consistent with the mass estimated from the stellar velocity dispersion. Notice that, in order for the black hole mass estimates from σ_* and from the virial assumption to be consistent with each other, one must have $\sin^2 i \geq 0.46$. In other words, under the assumption of a disc-like BLR geometry, $i \geq 43^\circ$. This provides further, independent support to the relatively high inclination we derive from the X-ray spectral analysis with the disc-reflection model. Hereafter, we assume that $M_{\text{BH}} = (4.5 \pm 1.5) \times 10^7 M_{\odot}$ and we refer to $M_{\text{best}} = 4.5 \times 10^7 M_{\odot}$.

6 LOOKING FOR A REVERBERATION TIME LAG

An inescapable consequence of interpreting the soft X-ray excess as partially ionized X-ray reflection off the inner accretion disc is that relatively short time delays are expected between X-ray energy bands dominated by the intrinsic power law, and bands dominated by disc-reflection (i.e. the soft excess). Such lags have been indeed discovered in the Narrow-Line Seyfert 1 galaxy 1H 0707-495 (Fabian et al. 2009), and subsequently confirmed to be present in many other sources (Emmanoulopoulos et al. 2011; de Marco et al. 2011; 2013; Kara et al. 2013a, 2013b; Cackett et al. 2013; Fabian et al. 2013). The interpretation of the soft X-ray lags as due to the delayed reflection off the inner accretion disc has then been confirmed thanks to the detection of very similar Fe K lags in

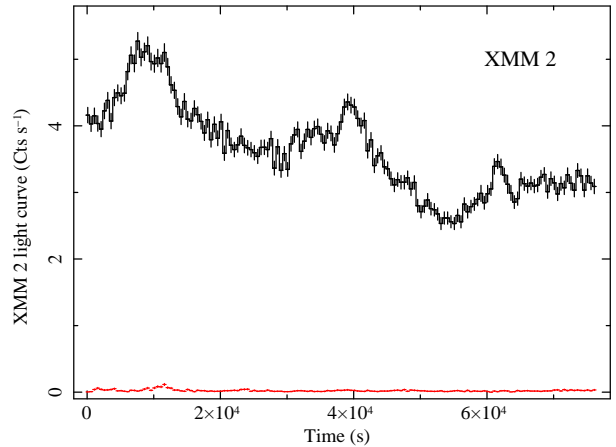


Figure 8. The broadband, 0.3–10 keV EPIC-pn light curve of ESO 362–G18 during the XMM 2 observation is shown with a bin size of 500 s. The corresponding background light curve is also shown for comparison.

some sources (Zoghbi et al. 2012; Kara et al. 2013c, Zoghbi et al. 2013), although other authors consider the detected soft lags spurious and thus physically meaningless (e.g. Miller et al. 2010; Legg et al. 2012).

ESO 362–G18 is X-ray variable during the long XMM 2 observation, and the broadband 0.3–10 keV light curve is shown in

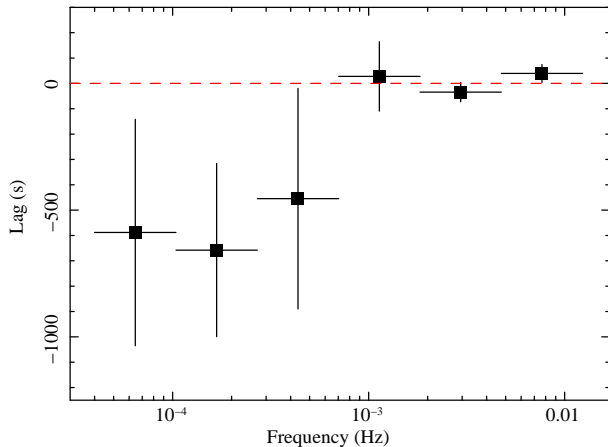


Figure 9. The lag–frequency spectrum of ESO 362–G18 between the 0.3–0.6 keV and the 0.8–3 keV bands. The lag is defined such that negative values mean that the softer (soft–excess–dominated) band lags the harder (likely continuum–dominated) one.

Fig. 8. The X–ray variability is of sufficiently high amplitude that lags between different energy bands can in principle be computed. To compute the lag–frequency spectrum, we select energy bands that, according to our best–fitting spectral model, are dominated by disc–reflection (0.3–0.6 keV) and by the intrinsic power law continuum (0.8–3 keV) respectively. In Fig. 9, we show the lag–frequency spectrum of ESO 362–G18 between the two selected energy bands, where negative (soft) lags mean that the soft band lags the hard one. We measure a soft lag of $|\tau| = 658 \pm 342$ s at $\nu \sim 1.7 \times 10^{-4}$ Hz. A similar lag is consistent to be present in the wide $0.4 - 7 \times 10^{-4}$ Hz frequency band. For $M_{\text{BH}} = M_{\text{best}}$, and assuming that soft lags are related to the light–crossing–time between the primary and reprocessed X–ray emission component (i.e. the power law continuum and the soft excess), the observed soft lag translates into a distance of $(3.0 \pm 1.5) r_g$ between the continuum and reflection emission sites. Dilution effects may slightly increase the intrinsic lag and thus the inferred distance between continuum and reprocessing sites (see e.g. Wilkins & Fabian 2013). By using the best–fitting spectral model discussed earlier, the fraction of the reflection and power law components in the two selected bands can be computed, and thus dilution effects can be taken into account. Using the same arguments of Wilkins & Fabian (2013), we infer an intrinsic lag of ~ 1600 s, corresponding to a distance of $\sim 7 r_g$ between the continuum and reflection emitting regions.

As mentioned, the latter result depends on the physical interpretation of the observed lag as a signature of reverberation. However, other interpretations (based on scattering and absorption) have been proposed (e.g. Miller et al. 2010). We cannot exclude that absorption variability contaminates our lag measurement, although the inspection of hardness ratios between different energy bands during the XMM2 observation, implies that spectral variability is confined within 5–10 %, i.e. absorption variability is only modest on short timescales.

7 ORIGIN OF THE VARIABLE ABSORBER AND CONSTRAINTS ON THE X–RAY EMITTING REGION(S) SIZE

The main result of our X–ray absorption variability analysis is that ESO 362–G18 makes a transition from a mildly absorbed state

with $N_{\text{H}} \simeq 5 \times 10^{21} \text{ cm}^{-2}$ and $C_{\text{f}} \simeq 0.5$ as observed during the *Swift* observation, to a highly absorbed one with $N_{\text{H}} \simeq 3 - 4 \times 10^{23} \text{ cm}^{-2}$ and $C_{\text{f}} \geq 0.94$ during the XMM 1 observation performed 63 days later

The observed X–ray absorption variability is most likely due to one absorber clump (cloud) crossing our line–of–sight during the XMM 1 observation. A clumpy absorber may be directly identified with the clumpy obscuring torus (e.g. Nenkova et al. 2008a; Rivers et al. 2011; Miniutti et al. 2014; Markowitz, Krumpke & Nikutta 2014). Another possibility is that the variable absorber is related to BLR clouds (e.g. Lamer, Uttley & McHardy 2003; Elvis et al. 2004; Risaliti et al. 2005, 2007, 2009; Sanfrutos et al. 2013; Miniutti et al. 2014). Although the BLR and clumpy torus are likely part of the same obscuring structure (Elitzur & Shlosman 2006), they can be physically distinguished by their dust content. The BLR is dust–free, which locates the BLR within the dust–sublimation radius. The same radius is instead generally considered as representative of the inner edge of the clumpy torus. To gain some insight on the location and origin of the variable absorber, we consider UV data of ESO 362–G18 with the goal of distinguishing between dust–free and dust–rich absorption during the XMM 1 observation.

7.1 UV variability

If the $3 - 4 \times 10^{23} \text{ cm}^{-2}$ absorber affecting the XMM 1 observation is associated with the dusty clumpy torus, the UV emission from ESO 362–G18 may also be affected, provided that the absorber covers a sufficiently high fraction of the UV–emitting region (likely the accretion disc). On the other hand, if the absorber is dust–free (e.g. the BLR clouds), no significant effect is expected in the UV. Reliable optical and UV fluxes can be obtained from the UVOT and OM telescopes on board *Swift* and *XMM–Newton* during the mildly absorbed (hereafter “unabsorbed” for simplicity) *Swift* and XMM 2 observations as well as during the absorbed XMM 1 one. The resulting optical/UV flux densities are given in Table 4.

The U and UVW1 fluxes are nearly consistent with being constant in all observations. On the other hand, the UVM2 flux is nearly the same during the unabsorbed *Swift* and XMM 2 observation, but ~ 30 per cent lower during the X–ray absorbed XMM 1 observation. The same is true for the UVW2 flux, which is ~ 40 per cent lower during the X–ray absorbed XMM 1 observation than during the unabsorbed *Swift* one (no data were collected in UVW2 during the XMM 2 observation).

It is worth pointing out that the UV intrinsic variability is an unlikely explanation for the observed variability in the UVM2 and UVW2 filters because the intrinsic X–ray luminosity is higher during the X–ray absorbed XMM 1 observation than during the two X–ray unabsorbed ones. The most natural interpretation of the observed UV variability is then that the UV–emission at the shorter wavelength UVM2 and UVW2 filters is affected by absorption (as are the X–rays) during the XMM 1 observation, while it is not during the two X–ray unabsorbed ones. By comparing the UV flux during absorbed/unabsorbed observations, and assuming that total coverage would completely block the UV emission, we infer that the absorber covers ~ 30 (~ 40) per cent of the UV–emitting region in the UVM2 (UVW2) filter. In summary, the UV data are consistent with a dusty absorber covering about 30–40 per cent of the UV emitting region during the X–ray absorbed XMM 1 observation. This strongly suggests that the absorber can be identified with one clump (or cloud) of the clumpy dusty torus, rather than with a BLR cloud.

Table 4. Flux densities in the UVW2 UVM2, UVW1, and U filters during the *Swift* and XMM 2 (X-ray unabsorbed) observations, and the XMM 1 (X-ray absorbed) one. Results are given in units of $10^{-15} \text{ erg cm}^{-2} \text{ s}^{-1} \text{ \AA}^{-1}$.

Filter	Swift ^a (unabsorbed)	XMM 1 ^b (absorbed)	XMM 2 ^b (unabsorbed)
UVW2	13.5 ± 0.6	7.9 ± 0.4	–
UVM2	12.2 ± 0.4	8.5 ± 0.4	12.4 ± 0.5
UVW1	11.8 ± 0.7	10.6 ± 0.5	9.9 ± 0.5
U	10.0 ± 0.5	10.7 ± 0.5	8.8 ± 0.4

^a The *Swift* UVOT filters are centered at 1928 Å (UVW2), 2246 Å (UVM2), 2600 Å (UVW1), and 3465 Å (U);

^b The *XMM-Newton* OM filters are centered at 2025 Å (UVW2), 2250 Å (UVM2), 2825 Å (UVW1), and 3450 Å (U).

7.2 The X-ray emitting region(s) size

As the UV are only partially covered during the XMM 1 observation with $C_{f, \text{UV}} \sim 0.3 - 0.4$, while the X-rays are fully covered with $C_{f, \text{X}} \sim 1$, the X-ray emitting region is significantly smaller in size than the UV emitting region. This is not highly surprising, and it is in line with the mounting evidence from e.g. microlensing results that X-rays originate in more compact, centrally concentrated regions of the accretion flow than optical/UV (e.g. Morgan et al. 2008; Chartas et al. 2009; Dai et al. 2010; Morgan et al. 2012; Mosquera et al. 2013). Further constraints on the X-ray emitting region size can be obtained from the X-ray absorption variability itself. As the X-ray emitting region is consistent with being fully covered during the XMM 1 observation ($C_f \geq 0.94$), one has $D_X \leq D_c$, where D_X and D_c are the assumed linear sizes of the X-ray emitting region and of the obscuring cloud respectively. On the other hand, $D_X = \Delta T v_c$, where v_c is the absorbing cloud velocity and $\Delta T \leq 63$ days is the time it takes to make the transition from an unobscured to a fully covered spectral state³.

As discussed above, the UV data strongly suggest that the absorbing structure can be identified with one cloud of the clumpy, dusty torus. Hence, v_c is lower than the Keplerian velocity at the dust sublimation radius $R_{\text{dust}} \sim 0.4 L_{\text{Bol}, 45}^{0.5} \text{ pc}$ (Nenkova et al. 2008a), where $L_{\text{Bol}, 45}$ is the bolometric luminosity in units of $10^{45} \text{ erg s}^{-1}$. The (averaged) bolometric luminosity of ESO 362-G18 can be estimated from the 2–10 keV luminosity assuming a X-ray bolometric correction k_{2-10} . We use here the total (rather than the power law) averaged and unabsorbed 2–10 keV luminosity $L_{2-10}^{(\text{tot})} \sim 5.1 \times 10^{42} \text{ erg s}^{-1}$, as material at R_{dust} sees all contributions. As for the X-ray bolometric correction, we assume $k_{2-10} = 25$ (Vasudevan et al. 2009), which gives $L_{\text{Bol}} = 1.3 \times 10^{44} \text{ erg s}^{-1}$ (i.e. an Eddington ratio of $L_{\text{Bol}}/L_{\text{Edd}} \simeq 0.02$ for a black hole mass of $M_{\text{BH}} = M_{\text{best}} = 4.5 \times 10^7 M_{\odot}$). From the estimated L_{Bol} we have that $R_{\text{dust}} \sim 0.14 \text{ pc}$. Assuming Keplerian motion of the clumpy torus clouds, one has that $v_c \leq 1180 \text{ km s}^{-1}$ for $M_{\text{BH}} = M_{\text{best}}$.

Substituting the upper limit on v_c into $D_X = \Delta T v_c$ gives $D_X \leq 6.4 \times 10^{14} \text{ cm}$. This corresponds to $D_X \leq$

³ Although the *Swift* observation is mildly absorbed, the large difference in column density with the XMM 1 observation excludes that the same structure was obscuring the *Swift* and XMM 1 observations. Hence, for the purpose of our discussion, the *Swift* observation is considered to be unabsorbed.

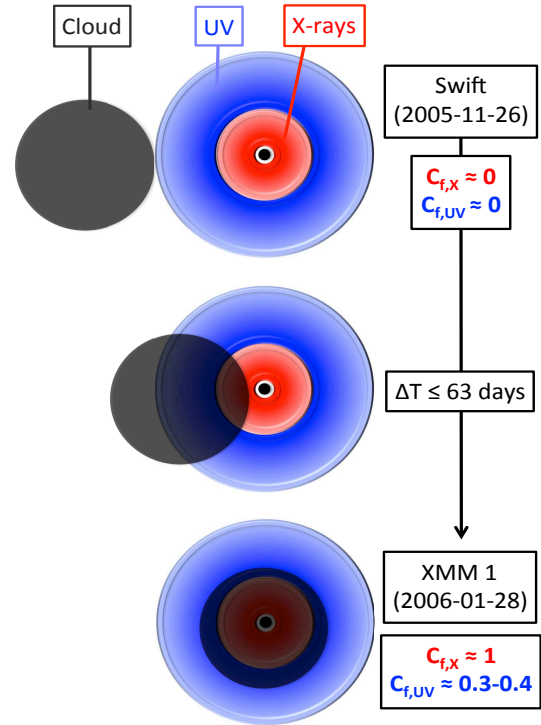


Figure 10. A simple sketch of the possible system geometry as a function of time during the transition between the unabsorbed *Swift* and the heavily absorbed XMM 1 observation. We show the larger UV-emitting region (blue in the on-line version), the smaller X-ray one (red in the on-line version), and the absorbing cloud (dark gray). The figure is not to scale for visual clarity. The time-evolution proceeds from top to bottom. The upper panel is representative of the unabsorbed *Swift* observation. The lower panel represents the likely geometry during the absorbed XMM 1 observation performed 63 days later, when the UV-emitting region is partially covered ($C_{f, \text{UV}} \sim 0.3 - 0.4$) by the dusty absorbing cloud, while the X-ray-emitting region is fully covered ($C_{f, \text{X}} \sim 1$). An intermediate situation where both the UV and X-ray-emitting regions are partially covered is shown in the middle panel.

$96 r_g M_{\text{best}}/M_{\text{BH}}$, so that X-rays come from radii within $D_X/2 = 48 r_g M_{\text{best}}/M_{\text{BH}}$ from the central, accreting black hole under the natural assumption of axial symmetry. This is consistent not only with microlensing results (e.g. Mosquera et al. 2013 and references therein), but also with measurements of the X-ray emitting size coming from other, better monitored X-ray occultation events which imply $D_X \leq 10 - 20 r_g$ (e.g. Risaliti et al. 2007, 2009; Sanfrutos et al. 2013). A simple sketch of the envisaged geometry and time-evolution is shown in Fig. 10.

The upper limit on D_X also represents a lower limit on D_c . By combining this with the maximum observed column density, we infer that the cloud number density is $n_c \leq 6.7 \times 10^8 \text{ cm}^{-3}$. Such a density is lower than that required for BLR clouds ($\geq 10^9 \text{ cm}^{-3}$, e.g. Davidson & Netzer 1979), supporting our identification of the variable absorber with one clumpy torus cloud.

8 DISCUSSION

Multi-epoch X-ray observations ESO 362–G18 reveal that the AGN is generally mildly absorbed by both partially ionized and neutral/low-ionization gas. While the warm absorber properties do not change significantly during our monitoring, the neutral absorber exhibits remarkable spectral variability with one observation (XMM 1) being highly significantly more absorbed than all others.

While unabsorbed, the X-ray spectrum is characterized by a strong soft excess, typical of the X-ray spectra of type 1 AGN. A broad feature is also seen at Fe K energies, and the *Suzaku* data from the HXD also exhibit a hard X-ray excess around 20–30 keV. All features are highly reminiscent of a reflection component off the inner accretion disc, whose spectral shape is distorted by relativistic effects. Using data from the two highest-quality, relatively unabsorbed observations *Suzaku* and XMM 2, we show that the X-ray spectrum is indeed best-described by a power law continuum affected by warm absorption, a reflection component from distant matter (comprising an unresolved Fe emission line) and, most importantly, a relativistically distorted disc-reflection spectrum originating in the inner accretion flow. Although its significance is rather low (about 2σ , see Fig. 9), an X-ray reverberation lag between the continuum- and disc-reflection-dominated bands supports our spectral model and suggests that the continuum and reprocessing sites are separated by $\sim 7 r_g$. From our disc-reflection model, we infer that the black hole powering the AGN in ESO 362–G18 is a rapidly spinning Kerr black hole, and we measure a black hole spin $a \geq 0.92$ at the 99.99 per cent (statistical) confidence level. The disc-reflection emissivity profile is steep, with $q = 4.3_{-0.6}^{+0.8}$, and the inclination i between the disc axis and our LOS is $53^\circ \pm 5^\circ$. Such a relatively high inclination implies that our LOS may intercept the classical obscuring torus of AGN unification schemes whose half-opening angle is typically assumed to be of the order of 45° .

Indeed, we observe X-ray absorption variability during our campaign, pointing to a clumpy nature of the cold absorber. All observations but one are consistent with being unabsorbed, or only mildly absorbed. The absorbed observation XMM 1 is characterized by a column density of $\sim 3 - 4 \times 10^{23} \text{ cm}^{-2}$ and a covering fraction of $C_f \geq 0.94$. On the other hand, the previous *Swift* observation performed only 63 days earlier is consistent with a typical mildly absorbed state, with a neutral column density about two orders of magnitude lower. UV variability between the absorbed XMM 1 and the unabsorbed *Swift* and XMM 2 observations strongly suggests that absorption is due to a dusty cloud of the clumpy torus transiting the LOS during the (only) heavily obscured observation of our monitoring campaign.

It is worth pointing out that, in our best-fitting spectral model, the absorber is applied to both the power law continuum and the disc-reflection component with the same covering fraction in each observation. We now perform a simple check of this assumption. We select the two most heavily absorbed observations (namely the XMM 1 and XMM 2 ones). Our best-fitting model, obtained by assuming the same covering fraction towards the two spectral components in each observation, results in $\chi^2 = 1634$ for 1579 dof. We then allow the covering fraction towards the power law and the disc-reflection component to be different. We reach a similar statistical quality ($\chi^2 = 1631$ for 1577 dof), and the covering fraction towards the two components is consistent with being the same during each observation. This means that any constraint that can be obtained on the size of the X-ray emitting region is valid for both spectral components.

The relatively short X-ray absorption variability timescale of ~ 2 months between the *Swift* and XMM 1 observations enables us to constrain the X-ray emitting-region size to $D_X \leq 96 r_g$, i.e. assuming the natural axial symmetry, $D_X/2 = R_X \leq 48 r_g$. As absorption affects both the power law continuum (X-ray corona) and soft excess (disc-reflection, according to our spectral decomposition), R_X has to be associated with the outer boundary of the largest of the two emitting sites. The resulting compact nature of the soft excess emitting-region is fully consistent with our interpretation in terms of disc-reflection as, according to our model (and the steep emissivity profile), the bulk of the X-ray reflection flux originates from radii within $\sim 10 r_g$. If the observed time lag between continuum and soft excess dominated energies can be interpreted roughly as the light-crossing-time between the continuum and soft excess emitting sites (a delay that would then correspond to a distance of $\sim 7 r_g$), our upper limit on the X-ray source size(s) is likely to significantly overestimate the real geometrical sizes.

As the X-ray source is consistent with being fully covered during the XMM 1 observation, the cloud linear size must be larger (or at most equal) to the X-ray source size. By combining this result with the observed column density we infer a cloud density of $n_c \leq 6.7 \times 10^8 \text{ cm}^{-3}$. Such a density is lower than that required for BLR clouds, supporting our identification of the variable absorber with one cloud of the dusty, clumpy torus.

9 CONCLUSIONS

In summary, ESO 362–G18 is a Seyfert galaxy characterized by an averaged bolometric luminosity of $1.3 \times 10^{44} \text{ erg s}^{-1}$ which, considering our best-estimate for the black hole mass of $4.5 \times 10^7 M_\odot$, translates into an Eddington ratio of 0.02. The X-ray spectrum comprises a reflection component off the inner accretion disc around an almost maximally spinning Kerr black hole, and we infer a disc inclination of $\sim 53^\circ$. Such high an inclination is expected to intercept, at least at times, the atmosphere of the obscuring torus which is generally thought to have an half-opening angle of $\sim 45^\circ$. Indeed, we detect variable X-ray absorption in our data, with the most remarkable event occurring over ≤ 2 months. The X-ray and UV data enable us to identify the variable absorber with the clumpy, dusty torus. The observed occultation event suggests that both the X-ray continuum and soft excess originate in a compact region within $\sim 50 r_g$ from the central black hole. This supports our view that the soft excess is due to relativistic disc-reflection off the partially ionized disc surface. The detection of a relatively short time lag between the continuum and the soft excess also supports this interpretation and the inferred continuum-to-reprocessor distance ($\sim 7 r_g$) may indicate that the actual size of the X-ray emitting region(s) is significantly overestimated by our upper limit.

ACKNOWLEDGMENTS

This work is based on observations obtained with *XMM-Newton*, an ESA science mission with instruments and contributions directly funded by ESA Member States and NASA. We made use of data obtained from the Chandra Data Archive, and software provided by the Chandra X-ray Center (CXC). We acknowledge the use of public data from the *Swift* data archive. This work also made use of data from the *Suzaku* observatory, a collaborative mission between the space agencies of Japan (JAXA) and the USA (NASA). This work has made use of data and/or software provided

by the High Energy Astrophysics Science Archive Research Center (HEASARC), which is a service of the Astrophysics Science Division at NASA/GSFC and the High Energy Astrophysics Division of the Smithsonian Astrophysical Observatory. This research was funded by the European Union Seventh Framework Program (FP7/2007–2013) under grant 312789. BAG thanks the Spanish MINECO for support through the FPI program associated with grant AYA2010-21490-C02-02. MS thanks the CSIC JAE-Predoc program for support. NLS acknowledges support by ESA through the ESAC trainee program.

REFERENCES

- Bennert N., Jungwiert B., Komossa S., Haas M., Chini R., 2006, *A&A*, 459, 55
- Bentz M. C. et al., 2009, *ApJ*, 705, 199
- Bianchi S., Miniutti G., Fabian A. C., Iwasawa K., 2005, *MNRAS*, 360, 380
- Bianchi S., Piconcelli E., Chiaberge M., Jimeénez-Bailón E., Matt G., Fiore F., 2009, *ApJ*, 695, 781
- Brenneman L. W., Reynolds C. S., 2006, *ApJ*, 652, 1028
- Cackett E. M., Fabian A. C., Zoghbi A., Kara E., Reynolds C.S., Uttley P., 2013, *ApJ Lett.*, 764, L9
- Chartas G., Kochanek C. S., Dai X., Poindexter S., Garmire G., 2009, *ApJ*, 693, 174
- Dai X., Kochanek C. S., Chartas G., Kozłowski S., Morgan C.W., Garmire G., Agol E., 2010, *ApJ*, 709, 278
- Davidson K., Netzer H., 1979, *Reviews of Modern Physics*, 51, 715
- de Marco B., Ponti G., Uttley P., Cappi M., Dadina M., Fabian A.C., Miniutti G., 2011, *MNRAS*, 417, L98
- de Marco B., Ponti G., Cappi M., Dadina M., Uttley P., Cackett E.M., Fabian A.C., Miniutti G., 2013, *MNRAS*, 431, 2441
- Elitzur M., Shlosman I., 2006, *ApJ Lett.*, 648, L101
- Elvis M., Risaliti G., Nicastro F., Miller J.M., Fiore F., Puccetti S., 2004, *ApJ Lett.*, 615, L25
- Emmanoulopoulos D., McHardy I. M., Papadakis I. E., 2011, *MNRAS*, 416, L94
- Fabian A. C. et al., 2009, *Nature*, 459, 540
- Fabian A. C. et al., 2013, *MNRAS*, 429, 2917
- Fraquelli H. A., Storchi-Bergmann T., Binette L., 2000, *ApJ*, 532, 867
- García-Rissmann A., Vega L. R., Asari N. V., Cid Fernandes R., Schmitt H., González Delgado R.M., Storchi-Bergmann T., 2005, *MNRAS*, 359, 765
- Kalberla, P. M. W., Burton, W. B., Hartmann, D., et al. 2005, *A&A*, 440, 775
- Kara E., Fabian, A. C., Cackett, E. M., Steiner J.F., Uttley P., Wilkins D.R., Zoghbi A., 2013a, *MNRAS*, 428, 2795
- Kara E., Fabian A. C., Cackett E. M., Miniutti G., Uttley P., 2013b, *MNRAS*, 430, 1408
- Kara E., Fabian A. C., Cackett E. M., Uttley P., Wilkins D.R., Zoghbi A., 2013c, *MNRAS*, 434, 1129
- Lamer G., Uttley P., McHardy I. M., 2003, *MNRAS*, 342, L41
- Laor, A. 1991, *ApJ*, 376, 90
- Legg E., Miller L., Turner T. J., Giustini M., Reeves J.N., Kraemer S.B., 2012, *ApJ*, 760, 73
- Maiolino R. et al., 2010, *A&A*, 517, A47
- Markowitz A. G., Krumpke M., Nikutta R., 2014, *MNRAS*, 439, 1403
- Marinucci A. et al., 2013, *MNRAS*, 429, 2581
- Merritt D., Ferrarese L., 2001, *ApJ*, 547, 140
- Miller L., Turner T. J., Reeves J. N., Braito, V., 2010, *MNRAS*, 408, 1928
- Miniutti G. et al., 2014, *MNRAS*, 437, 1776
- Morgan C. W., Kochanek C. S., Dai X., Morgan N. D., Falco, E. E., 2008, *ApJ*, 689, 755
- Morgan C. W. et al., 2012, *ApJ*, 756, 52
- Mosquera A. M., Kochanek C. S., Chen B., Dai X., Blackburne J.A., Chartas G., 2013, *ApJ*, 769, 53
- Nandra K., O’Neill P. M., George I. M., Reeves J. N., 2007, *MNRAS*, 382, 194
- Neškova M., Sirocky M. M., Ivezić Ž., Elitzur M., 2008a, *ApJ*, 685, 147
- Neškova M., Sirocky M. M., Nikutta R., Ivezić Ž., Elitzur M., 2008b, *ApJ*, 685, 160
- Park D., Kelly B. C., Woo J.-H., Treu T., 2012, *ApJS*, 203, 6
- Piconcelli E., Jimenez-Bailón E., Guainazzi M., Schartel N., Rodríguez-Pascual O.M., Santos-Lleó M., 2005, *A&A*, 432, 15
- Piconcelli E., Bianchi S., Guainazzi M., Fiore F., Chiaberge M., 2007, *A&A*, 466, 855
- Porquet D., Dubau J., 2000, *A&A Supplement*, 143, 495
- Puccetti S., Fiore F., Risaliti G., Capalbi M., Elvis M., Nicastro F., 2007, *MNRAS*, 377, 607
- Risaliti G., Elvis M., Fabbiano G., Baldi A. & Zezas, A. 2005 *ApJ*, 623, L93-L96
- Risaliti G., Elvis M., Fabbiano G., Baldi A., Zezas A., Salvati M., 2007, *ApJ Lett.*, 659, L111
- Risaliti G. et al., 2009, *ApJ*, 696, 160
- Risaliti G., Nardini E., Salvati M., Elvis M., Fabbiano G., Maiolino R., Pietrini P., Torricelli-Ciamponi G., 2011, *MNRAS*, 410, 1027
- Rivers E., Markowitz A., Rothschild R., 2011, *ApJ Lett.*, 742, L29
- Ross R. R., Fabian A. C., 2005, *MNRAS*, 358, 211
- Sanfrutos M., Miniutti G., Agís-González B., Fabian A.C., Miller J.M., Panessa F., Zoghbi A., 2013, *MNRAS*, 436, 1588
- Tremaine S. et al., 2002, *ApJ*, 574, 740
- Vasudevan R. V., Mushotzky R. F., Winter L. M., Fabian A. C., 2009, *MNRAS*, 399, 1553
- Wilkins D. R., Fabian A. C., 2013, *MNRAS*, 430, 247
- Winter, L. M., Mushotzky, R. F., Tueller, J., & Markwardt, C. 2008, *ApJ*, 674, 686
- Woo J.-H. et al., 2010, *ApJ*, 716, 269
- Xiao T., Barth A. J., Greene J. E., Ho L. C., Bentz M. C., Ludwig R. R., Jiang Y., 2011, *ApJ*, 739, 28
- Zoghbi A., Fabian A. C., Reynolds C. S., Cackett E. M., 2012, *MNRAS*, 422, 129
- Zoghbi A., Reynolds C., Cackett E. M., Miniutti G., Kara E., Fabian A.C., 2013, *ApJ*, 767, 121